

AERODYNAMIC AND AEROACOUSTIC ASSESSMENT OF 3D PRINTED AAM PROPELLER BLADES WITH SURFACE TREATMENTS

Dominik Skrna[1], Marcos de Rosa Jacinto[1], Lea Frei[1], Bernhard Mittenecker[1], Johannes Nagl[1], Helmut Mad[1] & Martin Berens[1]

[1]Technische Universität Wien. Lehárgasse 6, Vienna 1060, Austria.

Abstract

In this study, three off-the-shelf conventional Advanced Air Mobility (AAM) propeller blades in the diameter range from 20 to 24 inches are replicated via 3D-printing. Based on scanned geometry models, computational aerodynamic performance, aeroacoustic directivity and SPL spectra, as well as structural analysis reports are obtained. Several post-processing technologies are applied to the 3D-printed PLA blades to improve the surface properties, including sanding, spray coating and chemical treatment. The experimental campaign measurements indicate that the thrust of the 3D-printed replicas was lower when compared to the original blades at the same rotational speed, while for specific surface-treated blades, the respective torque was reduced. The acoustic output reveals that across all three propeller geometries, the 3D-printed blades can lead to OASPL reductions at multiple operating points compared to the original CFRP and injection-moulded versions, regardless of the microphone position. The most promising aerodynamic and aeroacoustic performance was achieved by the variants that were sanded to 400-grit and subsequently coated.

Keywords: 3D-printing. Propeller blades. Advanced Air Mobility. Surface modifications.

1. Introduction

Additive Manufacturing (AM) has emerged as a promising approach for the rapid prototyping and low-volume production of aerospace components, including propeller blades for AAM applications. However, the surface quality, geometric fidelity and structural behaviour of 3D-printed components often differ significantly from those of conventionally manufactured propellers, directly affecting aerodynamic performance and acoustic emissions [1]. This study aims to evaluate the effectiveness of selected post-processing strategies applied to Fused Deposition Modelling (FDM) 3D-printed AAM propeller blades in reproducing the performance parameters of the original propellers. The objective of applying those treatments is to improve the surface quality by reducing roughness, caused by 3D-printing layer lines, and by removing any irregularities and defects.

The original reference propeller blades were manufactured through different technologies, namely injection moulding and hand lamination, including subsequent curing. Accordingly, materials with varying mechanical properties were used, which is why structural limitations are expected for the 3D-printed replicas. Therefore, a Finite Element Method (FEM) analysis is carried out to assess the structural properties of the AM blades compared to the original ones. The material properties of the filament used (PLA) are determined by tensile tests with corresponding directional characteristics. Additionally, Computational Fluid Dynamics (CFD) and Computational Aero-Acoustics (CAA) data are obtained to provide the respective load data for the structural analysis and to validate the experimental results.

The combined numerical and experimental approach aims to demonstrate that appropriately post-processed AM propeller blades can closely replicate the aerodynamic and acoustic characteristics of the original propeller, supporting their potential use in AAM development and testing.

https://doi.org/10.71945/icas2026_0195

2. Literature Review

Investigations into the aerodynamic effects of surface irregularities, caused by ice and dirt build-up as well as protrusions from manufacturing, started in the late 1930s. NACA´s special Report 78 [2] used varying methods of surface preparation to introduce irregularities to investigate the adverse effects of surface roughness on aerodynamic performance, especially drag increase. It was concluded that drag due to rough surfaces is dominant at high free-stream velocities and diminishes at lower speeds. Furthermore, it was stated that grain-sized irregularities, with dimensions smaller than 0.1 mm, can already increase the drag coefficient by up to 63%. Those conclusions emphasise the necessity of surface treatments of 3D-printed propellers.

More recent studies, which focused on 3D-printed propeller blades with diameters up to 14 inches [3], have concluded that surface roughness and trailing-edge thickness strongly influence propeller efficiency. Research on AM propellers has shown performance penalties of up to several percent in thrust and propeller efficiency compared to injection-moulded or hand-laminated blades made of Carbon Fibre Reinforced Polymers (CFRP), primarily due to layer-induced roughness and dimensional deviations [4]. Comprehensive studies combining high-fidelity numerical aeroacoustic simulations with experimental validation of 3D-printed propeller blades remain limited, particularly in the context of AAM-relevant operating conditions. Recent research on the acoustic emissions of 3D-printed propellers [1, 5] has focused on significantly smaller propeller diameters at higher rotational speeds than those considered in this paper. Nevertheless, the results indicate that surface roughness represents a significant contributor to decibel variations in the tonal and broadband noise range.

Various post-processing techniques for 3D-printed parts have been investigated in literature, including sanding, surface polishing, chemical smoothing and coating. According to the selected printing process and the used printing material, the efficiency, time and costs required for the individual post-processing techniques can be assessed [6]. In this paper, in addition to sanding and coating, special focus is placed on smoothing the surfaces of the blades using Tetrahydrofuran (THF). Besides treating the blades in a vapour chamber, in which the samples are exposed to the gases of the chemical for several hours, a manual application of specific chemicals on the 3D-printed parts can also lead to improvements of surface roughness. This was demonstrated in a study by [7], in which Acetone was applied on Acrylonitrile Styrene Acrylate (ASA) 3D-printed parts. This fluid, which serves as a solvent for the top layer, contributed in reducing the height differences on the surface caused by the layer lines by transferring dissolved material into these troughs. However, an extended exposure time or too many treatments can also significantly alter the mechanical properties and change the dimensions and shape of the specimen [8].

3. Methodology

In this paper, a holistic approach is carried out, starting with high-fidelity numerical simulations to obtain aerodynamic performance and aeroacoustic noise data, which serve as a reference for the experimental campaign. To provide a representative comparison between computational and experimental data, the original reference propeller blades were 3D-scanned, and mesh inaccuracies were corrected. Before manufacturing the blades, the structural properties at predefined load cases are assessed in order to verify tip deflections and ensure safe operations during the experimental campaign. Finally, the post-processing techniques are applied, and the resulting surface roughness for each case is measured.

3.1 Reference propeller geometry data

In this study, three different baseline propeller blade geometries from the manufacturers Advanced Precision Composites (AP 20x13E CCW), Mejzlik Propellers (MP-FA 22x7.4 CCW) and T-MOTOR (TM-FA 24.2x7.9 CCW) are used as reference configurations. All of them are two-bladed and rotate counter-clockwise (CCW). The MP-FA and TM-FA propellers, which are both foldable, are made out of a CFRP shell and a foam core, creating a lightweight and high-stiffness sandwich composite. In contrast, the original AP propeller was manufactured using injection moulding technologies with additional glass-fiber (GF) reinforcement in the nylon pellets [9].

Propeller	**AP**	**MP-FA**	**TM-FA**
Diam. [inch]	20	22	24.2
Pitch [inch]	13	7.4	7.9
Materials	GF Nylon	CFRP-Foam	CFRP-Foam
Mass [g]	97.1	76.9	92.6
Ra [μm]	4.16	3.38	2.05
Solidity [-]	0.072	0.075	0.085
ρ_{av} [kg/m^3]	1718	791	655

Table 1 – Properties of each reference propeller.

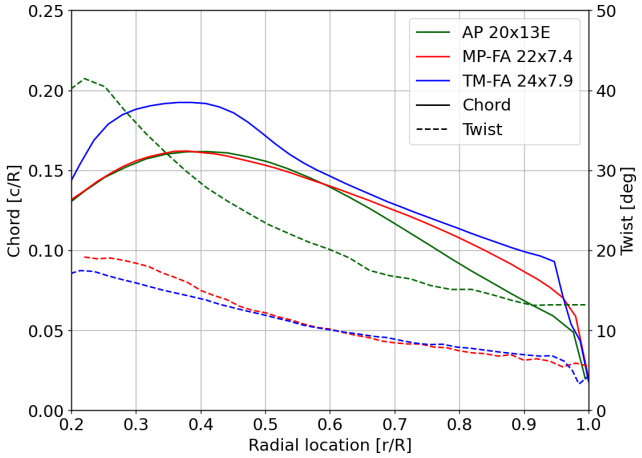


Figure 1 – Chord length (c/R) and twist distribution of all three investigated geometries.

In Tab. 1, properties of all three reference propellers are summarised. The surface roughness data (Ra) were obtained using a Keyence 3D laser scanning microscope. A representative surface area at a predefined radial and chord-wise position was selected for data recording at a magnification factor of five, using a circular measurement path.
The reference propellers were 3D-scanned in an industrial ZEISS METROTOM computer tomography system to obtain a precise CAD model. Due to measurement space constraints, only half of each propeller, respectively, one blade, could be measured. Subsequently, information about the twist and chord distribution of those propeller blades was derived from the CAD models and is displayed in Fig. 1. The chord length data, which are displayed as solid lines and which are referenced to the respective propeller radius *R*, are very similar for all baseline geometries. However, the TM-FA blade is expected to generate more thrust, because next to the larger diameter, the relative chord length (c/R) exceeds that of the other blades for radial locations below 0.6 r/R. The comparison of the solidity values stated in Tab. 1 confirms this assumption. With regard to the twist characteristics, the AP geometry represents an exception, as the twist angle is, independent of the radial position, on average twice as high as for the CFRP composite propellers. Furthermore, if not given by the manufacturers, the profiles at multiple cross-sections were assumed to be typical airfoils used for AAM propellers, namely NACA 4409 and NACA 4412. In case multiple profiles were applied at different radial positions, a linear interpolation between the airfoils was conducted.
Despite mesh clean-up and de-featuring efforts, some inaccuracies in the surface quality of the scanned data could not be completely removed. It was therefore necessary to rebuild the propeller geometries to obtain better aerodynamic surface properties, which are required for experimental validation. This was done using an in-house Python script for blade generation. Since exact dimensional accuracy between these two versions was not possible to achieve, both blades were computationally assessed. In Fig. 2, the comparison of the scanned and rebuilt CAD geometries is displayed.

3.2 Material characterisation

In Tab. 2, the properties of all relevant applied materials are summarised. Since material data were not available from all propeller manufacturers, the table was completed with representative data from the Ansys material database [10]. The two CFRP composite propellers, which vary in density, could either have been manufactured using different laminate thicknesses or varying material combinations. For the sake of simplicity, it was decided to use the same material data but to vary the thicknesses of the CFRP material layers, related to the overall averaged density values.
In the data sheet of the PLA manufacturer [11], the properties for a horizontally and vertically printed specimen were given, stating that printing the probes vertically results in higher strength and modulus values than a flat printed specimen. As the printing settings selected for the propellers varied from those specified in the data sheet, it was decided to conduct independent tensile tests on the corresponding specimens for the characterisation of the actual material properties. The probes were

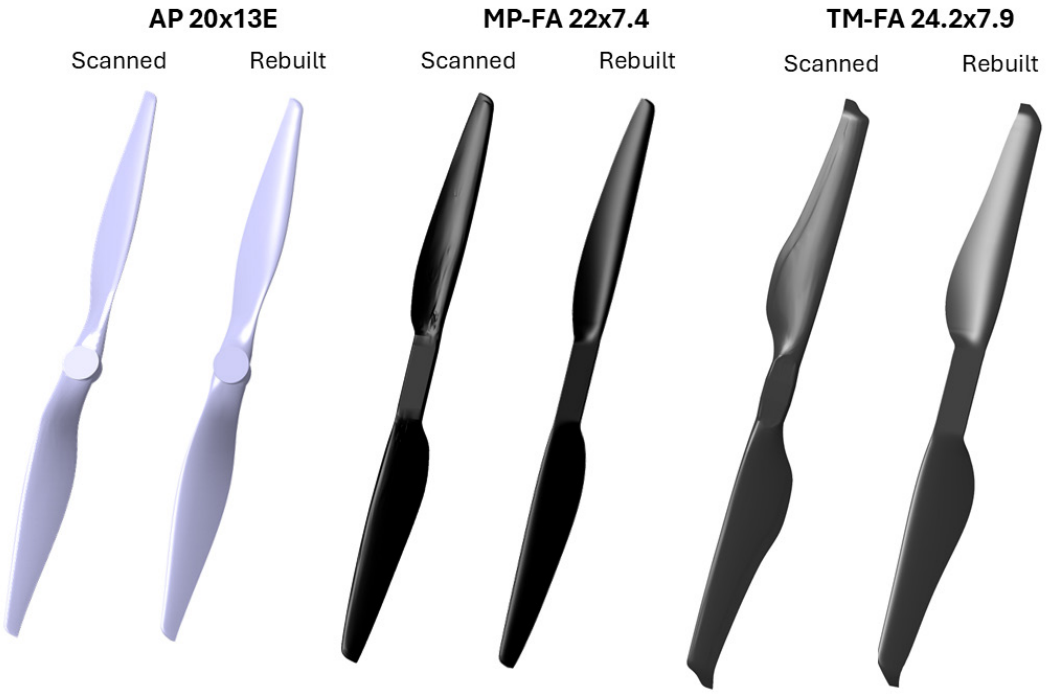


Figure 2 – Scanned and rebuilt versions of the three investigated propeller geometries.

3D-printed and tested according to DIN EN ISO 527-2 [12] to capture the respective anisotropic effects of the selected additive manufacturing process. In addition to the orientation, the number of perimeters and the infill density of the specimen were also adjusted to ensure that these values correspond to the settings applied to the 3D-printed propellers. For material characterisation, an electric tensile test stand was used, and the corresponding elongation was measured with an extensometer. All specimens showed similar failure locations after testing.
The resulting mechanical data, including tensile elastic modulus (E_t) and tensile strength (σ_y, t), were evaluated according to the equations given in DIN 527 and subsequently used to define direction-dependent material properties for the numerical model. These experimentally derived parameters served as the basis for the structural analysis of the propeller blade geometries using FEM, ensuring that the tip deflection behaviour of the component was represented realistically with respect to the actual printing orientation. Additionally, the flexural modulus (E_f) and the respective flexural strength ($\sigma_{y,f}$) as well as the elongation at yield point (ε_y) data are listed, which are relevant for a safe operation assessment. Since no material testing in accordance with ISO 178 has been performed, the relevant data were obtained from the PLA manufacturer.

3.3 Computational setup

Aerodynamic and aeroacoustic simulations are performed using SIMULIA PowerFLOW [13], a Lattice-Boltzmann-Method (LBM) based solver, which is well suited for resolving unsteady flow features and noise generation mechanisms around rotating propellers. The solver applies a very large eddy simulation (VLES) framework, resolving larger turbulent structures while modelling unresolved scales. Far-

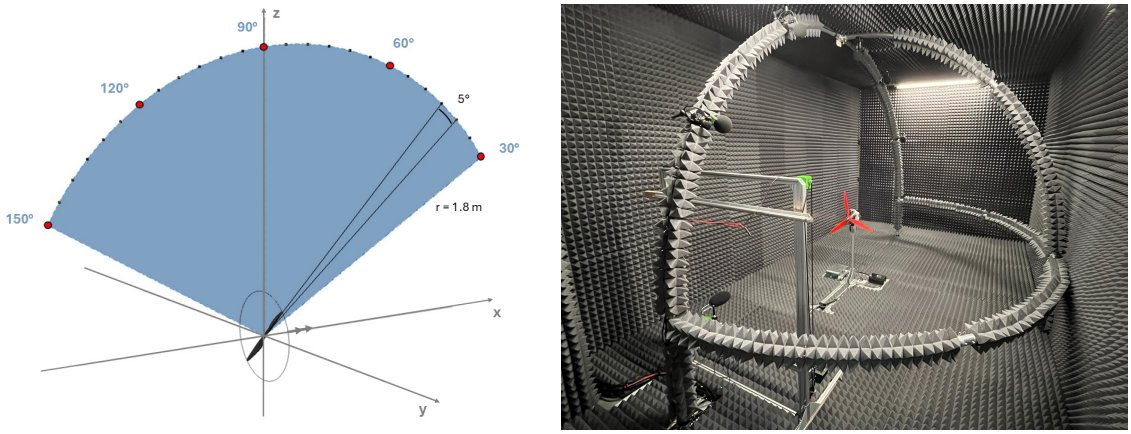
Table 2 – Material properties of the investigated propeller blades.

Material	$\rho[kg/m^3]$	$E_t[GPa]$	$\sigma_{y,t}[MPa]$	$E_f[GPa]$	$\sigma_{y,f}[MPa]$	$\varepsilon_y[\%]$
PLA (manufacturer) [11]	1240	2.30	51.00	3.15	81.0	2.90
PLA (specimen)	1179	1.78	36.95	-	-	2.60
GF Nylon [9]	1718	8.20	124.11	8.95	199.8	4.00
CFRP-Composite Laminate [10]	1490	121	2230	125	1800	1.67
CFRP-Composite Foam [10]	80	0.102	3.05	0.105	3.15	20.00

field acoustic quantities are evaluated using the permeable formulation of the Ffowcs Williams–Hawkings analogy. A cylindrical control surface with a diameter 60% larger than the one of the propeller encloses the source region. Sound Pressure Level (SPL) spectra and Overall Sound Pressure Level (OASPL) directivity patterns are computed using an array of observer points distributed at 5° intervals in a plane perpendicular to the rotational one (XZ), at a radial distance of 1.8 m from the propeller center. The observer positions were adjusted to match the microphone locations in the sound measurement room, with 180° representing the front of the propeller. The experimental microphone locations are situated at 30°, 60°, 90°, 120° and 150°. Those observer positions are highlighted in red in Fig. 3a, which displays an overview of the computational setup.
Previous work by Grande et al. [14] has identified Laminar Separation Bubble (LSB) formation as a key contributor to broadband noise in low Reynolds number propeller flows. To capture these effects, the natural boundary layer transition model available in PowerFLOW was activated. To ensure numerical accuracy, a comprehensive mesh refinement study was conducted. A total of 14 refinement levels were evaluated, with the finest configuration (VR13) achieving a resolution of 170 voxels along the airfoil chord. This corresponds to a minimum voxel size of $1.76 \cdot 10^{-4}$ m. Acoustic data acquisition begins after an initial transient period, once thrust and torque signals reach steady-state convergence. The sampling duration corresponds to ten complete propeller revolutions. A maximum resolved frequency of 25 kHz is selected in accordance with the Nyquist criterion, using a factor of two for adequate signal resolution. The frequency resolution is set to 13.3 Hz, equivalent to one-tenth of the blade passing frequency at 4000 RPM. On average, each simulation requires approximately 7680 core hours. The infrastructure available in the Austrian Scientific Computing (ASC) facilities was used to meet this computational demand.

3.4 Experimental validation

Experimental validation was conducted in the sound measurement room of the institute, shown in Fig. 3b, where thrust, torque, and acoustic pressure spectra were measured for hovering operating conditions, corresponding to an advance ratio of zero. A microphone array, consisting of five 1/2" CCP free-field GRAS 46AE microphones with a constant distance of 1.8 m to the source, is used to capture both tonal and broadband noise components. This non-certified test chamber, in which space constraints made it impossible to place the propeller directly in the center of the room, is primarily used to conduct relative comparisons of specific geometries. The influence of asymmetric recirculation patterns on the measurement results cannot be ruled out, so comparisons with computationally generated data are only possible to a certain extent. Nevertheless, the measurement microphones are aligned with the computational observer locations in the acoustic far field. Inside the measurement room, pyramid-shaped absorbers cover all walls, resulting in a cutoff frequency of 1225 Hz and a reverberation time of 0.12 seconds. Additionally, a camera was placed directly above



(a) Computational setup displaying all observer locations.

(b) Propeller test rig in the sound measurement room of the institute.

Figure 3 – Computational and experimental setup.

the propeller, next to the microphone at 90°, in order to measure tip deflections of the propeller blades during operation.
The operating points were systematically targeted by means of precise electronic speed rate control for the corresponding rotational velocities. The values were obtained using an ascending and descending sequence, maintaining the targeted RPM value for several seconds to allow for the acoustic measurements to be carried out, and to ensure sufficient data sampling for averaging. The acoustic measurement settings regarding frequency span and resolution, as well as measurement time, were selected accordingly in order to provide a match as close as possible to the computational setup. However, due to limitations of the measurement software and varying operational conditions, it was not always possible to align the frequency discretisation with the BPFs.

4. Manufacturing

In this chapter, details about the 3D-printing process and the subsequent surface treatment techniques are given. For each propeller geometry, seven configurations are tested, including the original reference propeller, an as-printed AM propeller, and five post-processed 3D-printed propellers. Various surface treatment techniques were applied individually and combined, including sanding, coating and chemical smoothing.

4.1 3D-printing process

The propeller blades were 3D-printed using filament extrusion based on the FDM technique. For this process, a Prusa XL FDM 3D-printer with a 0.4 mm nozzle diameter and 0.15 mm layer height, which is necessary to reproduce the detailed geometry, was selected. The infill percentage was set to 100% and the respective layers were aligned parallel to the radial axis of the blade, resulting in a printing time of about 4 hours per blade. Due to the limited printing volume and in order to avoid manufacturing-related defects, each blade was printed separately, oriented from the leading-edge to the trailing-edge. For the foldable propellers, parts of the original hub were used to assemble the FDM propellers. In the case of the AP blades, a simple hub concept was developed, and screws were used to connect the blades to the hub.
Before testing the propellers, static balancing was carried out. In case an imbalance was detected, the respective post-processing technique, which was applied to the blade beforehand, was used to add or remove mass. Accordingly, it was possible to control the mass distribution without modifying the surface with external materials or additional treatments. As already stated in the material characterisation chapter, the original PLA filament of the 3D-printer manufacturer was selected.
Initially, it was also planned to produce these blades using Acrylonitrile styrene acrylate (ASA). However, due to thermal deformation during the post-print cooling process, also known as warping, it was not possible to ensure the propeller geometry maintained its original shape. Attempts were made to slow down the cooling process by using an enclosure and prolonging the heating of the printing chamber, but these measures only marginally improved the results. Reducing the infill density can help to mitigate thermal stresses, however, the material properties of ASA are considerably inferior to those of PLA.
The main reason for working with ASA was the chemical post-processing of the surface using acetone, as this liquid has no noticeable material-dissolving effects on PLA. However, during the course of working on this topic, it became apparent that another chemical solvent, namely Tetrahydrofuran (THF), achieves similar results with PLA as acetone does with ASA. Therefore, the original idea of chemical surface treatment is being further investigated without the need to change the material.

4.2 Post-processing of the blades

NACA´s special Report 78 [2] not only describes the effects of surface irregularities on aerodynamic performance, but also provides guidelines for respective surface treatment. It is stated that smoothing the first quarter chord of the surface can halve the drag. As a result, special attention must be paid to the surface treatment of the leading edge. Additionally, the report states that smoothing a spray-painted surface with 400-grit sandpaper yields a surface equal in quality to highly polished metal. Therefore, each post-processing treatment starts with sanding the 3D-printed blade to at least a 400-grit level. To determine whether further sanding could improve the performance output, additional

propeller blades were also processed using grit sizes up to 1200. By applying the coating technique, the gaps between the layer lines are closed with spray putty. The blades were treated in successive spraying steps to ensure uniform application. However, care was taken to use as little as possible, as otherwise the weight of the blade would have increased significantly. Finally, a varnish spray was applied to create a protective layer on the surface.
For the third post-processing technique, the application of THF, both safety and processing time considerations were necessary in order to protect individuals and limit material loss. The initial plan was to place the propellers in a sealed chamber, where they would be exposed to THF vapours for several hours. Based on the findings from previous tests, namely significant deterioration in material properties due to plastic softening, it was decided to employ both spray and liquid brushing applications. For this purpose, the blades were treated on both sides with a minimal amount of THF and were afterwards hung up to air dry. This resulted in temporarily dissolving the outer layer without compromising the structural properties.
In Tab. 3, the applied surface treatments as well as mass and surface roughness of each blade case are summarised. For the naming convention, the designations of the three reference propellers were expanded to include the sanding grit number and the corresponding surface treatment abbreviation.

Table 3 – Naming convention and properties of each 3D-printed propeller case.

Case	Post-processing treatment			Properties	
	Sanding	Coating	THF	Mass [g]	Ra [μm]
AP-unmod.	-	-	-	81.2	10.11
AP-400	400	-	-	80.3	3.34
AP-400-coat.	400	X	-	82.4	4.85
AP-400-THF	400	-	X	82.5	3.54
AP-1200	1200	-	-	80.2	1.24
AP-1200-coat.	1200	X	-	84.3	5.20
MP-FA-unmod.	-	-	-	97.3	7.47
MP-FA-400	400	-	-	96.6	3.52
MP-FA-400-coat.	400	X	-	99.4	2.48
MP-FA-1200-THF	1200	-	X	97.3	8.10
MP-FA-1200	1200	-	-	96.1	1.86
MP-FA-1200-coat.	1200	X	-	100.5	3.39
TM-FA-unmod.	-	-	-	123.4	8.04
TM-FA-400	400	-	-	122.9	3.42
TM-FA-400-coat.	400	X	-	126.9	4.61
TM-FA-400-THF	400	-	X	124.3	5.28
TM-FA-1200	1200	-	-	122.4	3.80
TM-FA-1200-coat.	1200	X	-	126.7	5.11

When comparing the masses of the 3D-printed propellers with those of the conventional variants, given in Tab. 1, it can be seen that the 3D-printed versions of the CFRP composite propellers are on average 27% (MP) and 34% (TM) heavier. However, compared to the injection-moulded propellers (AP), the 3D-printed models show an average mass reduction of 16%. At this point, it must be noted that, due to the different hub connections of the conventional and 3D-printed versions of the propellers, a direct comparison of the masses based on the density data given in Tab. 2 is not applicable.
As expected, the sanding process reduced the blade mass. Since this is a manual process that depends largely on the operator's subjective assessment of surface finish during treatment, the amount of material removed varied from blade to blade. Nevertheless, a time limit was set for each sanding step, and a respective workflow was established to ensure that all propellers were processed uniformly. For the more finely sanded blades, a further reduction in mass was recorded. In contrast, the coating process resulted in a significant increase in mass despite the preceding sanding. Although once again a predefined procedure was followed when applying the coating, variations in the total mass of each propeller are inevitable. Furthermore, the chemical treatment also resulted in small increases in mass.

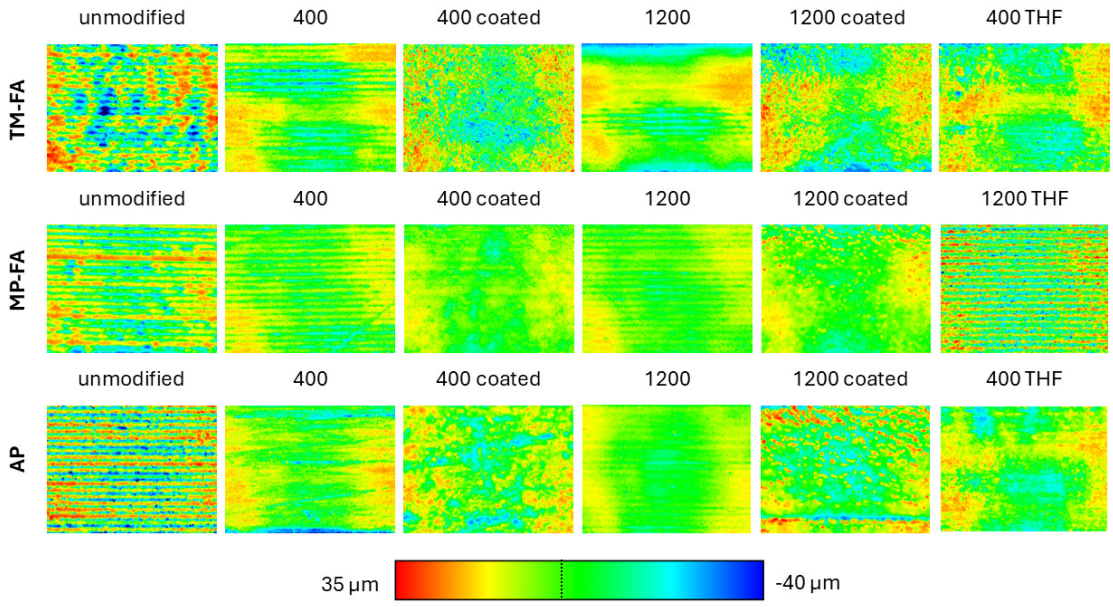


Figure 4 – Surface roughness comparison of the 3D-printed cases.

One parameter to characterise the degree of each post-processing technique is the surface roughness. The surface of each blade was scanned using a Keyence 3D laser microscope at approximately the same reference position to obtain the respective values. Compared to the relatively low surface roughness data of the conventional propellers, as given in Tab. 1, the unmodified 3D-printed propellers achieved significantly higher values, primarily due to the presence of individual printing lines. This is also evident in Fig. 4, which displays the laser scanning microscope images of all 3D-printed propeller blades. The radially oriented 3D-printed perimeters are visible as horizontal layers in this figure. While the sanding process reduced the height differences between each layer, the characteristic parallel pattern of the application scheme remains visible. Since the same sanding process was applied to each individual blade, the surface quality can be assumed to be comparable in this respect.
By coating the surface using spray putty, a grainy and blistered surface appears in the microscope image. On the one hand, this suggests the presence of tiny air bubbles trapped within the material. As the spray putty dries, these bubbles do not evaporate completely, leaving behind spherical structures. On the other hand, small clusters of particles can form in the spray can due to insufficient shaking before application, or on the PLA component due to insufficient distance during the spray application. Nevertheless, the layer lines resulting from the 3D printing manufacturing are barely visible in the final product.
The chemical treatment results in different surface qualities for the investigated geometries. While the AP and TM-FA propeller blades were sanded to 400 grit before the application of THF, the MP-FA propeller was smoothed to 1200 grit. The microscope image indicates that this additional, finer processing does not yield an improved surface structure, as the layer-line pattern is visible again, similar to the unmodified surface. Finally, in Fig. 5, all 3D-printed and post-processed propeller versions are displayed in comparison to the conventional blades. The colours of the filament were selected based on availability, however, the light grey propellers indicate the coated ones.

5. Computational study results

The computational study results are evaluated first to obtain an overview of the theoretical aerodynamic and aeroacoustic performance variations. The CFD, CAA and FEM simulations were carried out using processed and rebuilt versions of the individual scanned propeller blade geometries.

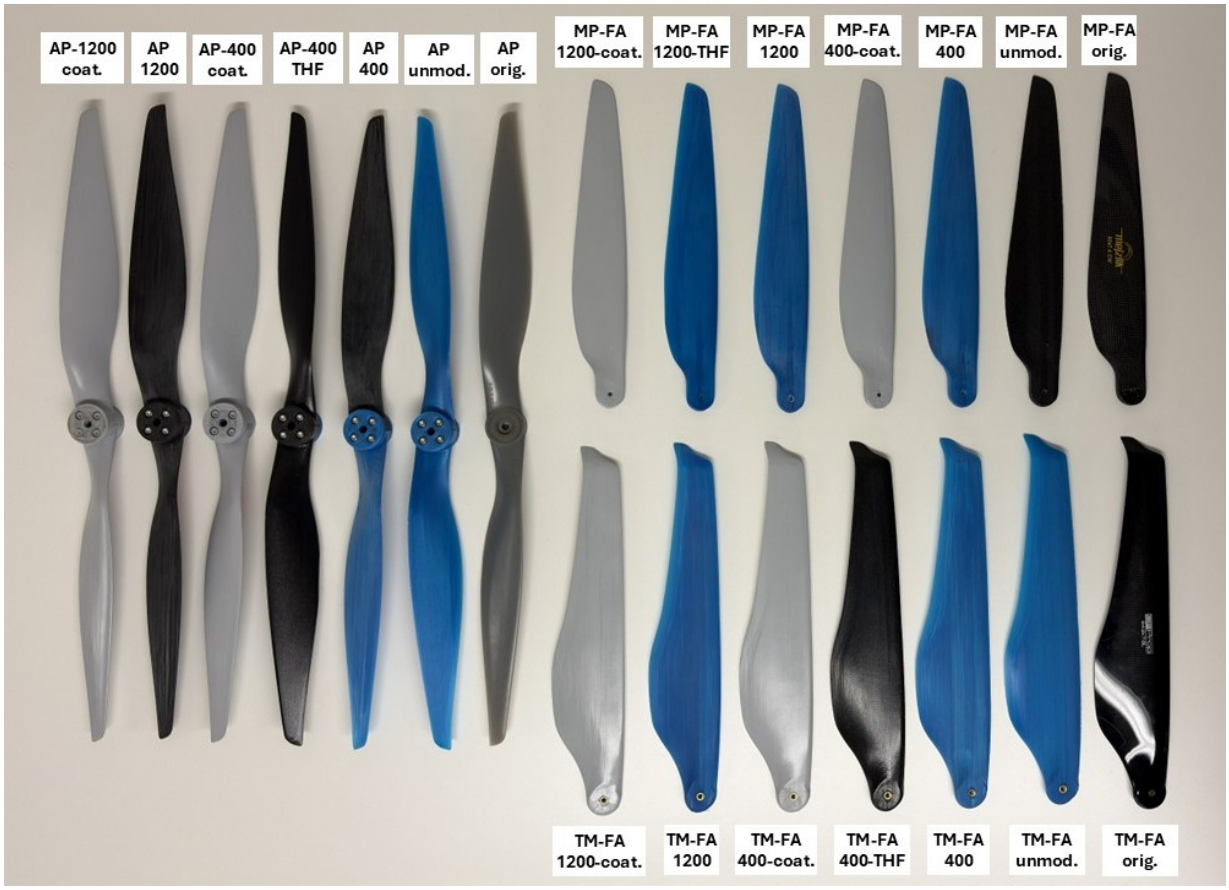
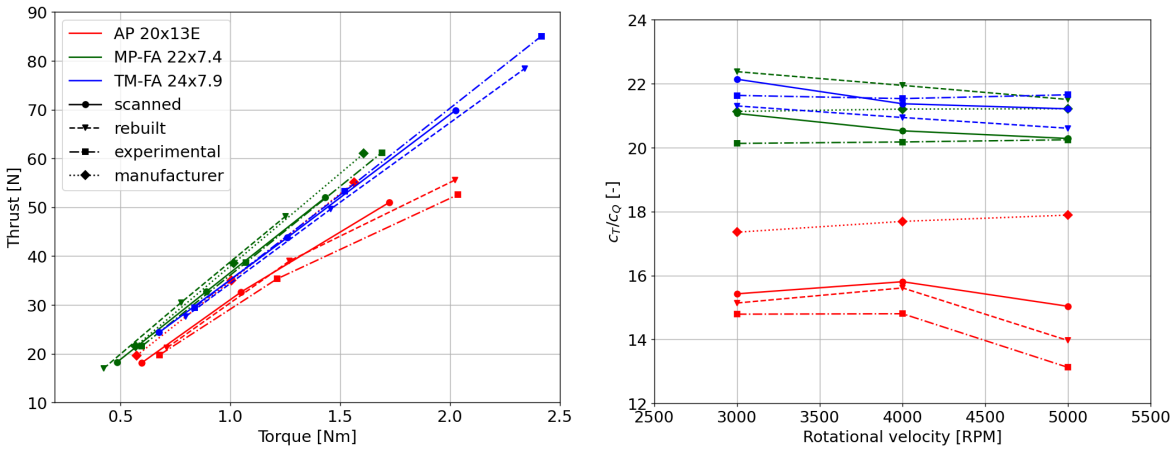


Figure 5 – All 3D-printed and original propeller blades of the AP, MP-FA and TM-FA configuration.

5.1 Aerodynamic performance results

In Fig. 6a, the computational thrust results of the scanned and rebuilt geometries, as well as the experimental data of the original reference blades, are plotted over the torque values, which are required to obtain the respective rotational velocity. Additionally, the data provided by the manufacturer for the AP and MP-FA cases are displayed. Each data set consists of three reference points, representing the output at 3000, 4000, and 5000 RPM.

It can be seen that the scanned propeller blade geometries can reproduce the experimentally obtained data to a certain level. However, especially for the TM-FA geometry, a significant reduction



(a) Thrust plotted over torque.

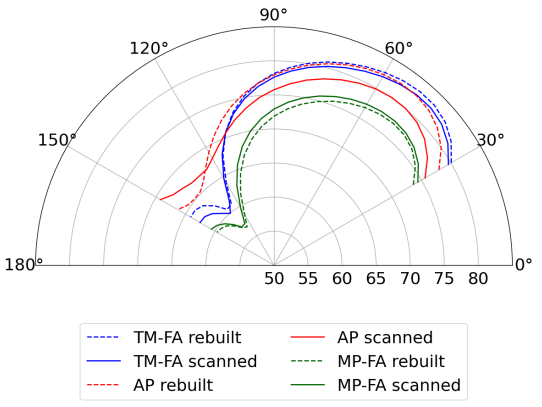
(b) c_T/c_Q results at multiple rotational velocities.

Figure 6 – Computational and experimental thrust, torque and c_T/c_Q results for multiple RPM values, including data provided by the manufacturer.

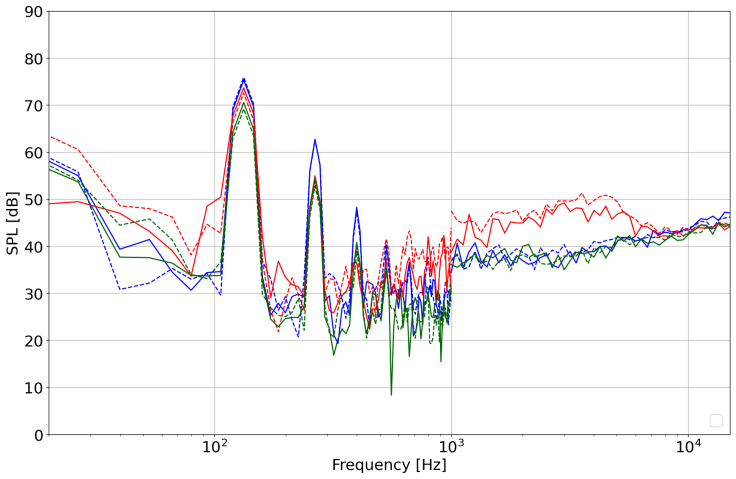
in thrust and torque is visible. On the other hand, the results of the rebuilt versions are mostly comparable with the experimental results, only the MP-FA propeller case shows significantly lower performance output. This highlights once again the problems associated with reproducing results that are not based on exact geometric data. Despite precise scanning of the geometry and derivation of the corresponding geometric parameters, proper representation and implementation of the propellers for numerical simulations is only partially achievable.
With regard to the AP propeller performance data provided by the manufacturer, it is important to note that, although these values clearly differ from the computational and experimental data shown in Fig. 6a, the discrepancy primarily refers to the differences in the torque values. This is evident when looking at the respective thrust to torque coefficient ratios (c_T/c_Q), which are plotted over the rotational velocity in Fig. 6b. These offsets in the data can be explained by differences in drivetrain configurations or simulation boundary conditions, as determined by the methodology used to generate these data. In contrast, the MP-FA propeller performance data provided by the manufacturer match very well with the experimentally obtained results of this paper.

5.2 Aeroacoustics output

In Fig. 7a, the computational OASPL results of all three reference geometries are given for a rotational velocity of 4000 RPM. While the scanned and rebuilt versions match very well for the MP-FA and TM-FA propeller geometries, a clear offset is evident between the computational results of the two AP propeller versions. The reason for this becomes evident when looking at the corresponding SPL spectra graph for an observer at 90° in the rotational plane, plotted in Fig. 7b. A clear increase in broadband noise is observed for the rebuilt version of the AP propeller. The directivity and spectral plots at the other investigated rotational velocities indicate a similar pattern.
In order to comprehensively represent and to facilitate the broadband noise data distinction between the cases, in the SPL spectra graphs, results above 1 kHz are filtered in 1/12th octave bands, indicated by dashed lines, as displayed in Fig. 7b. The solid lines shown for frequencies below 1 kHz indicate the data obtained with the targeted frequency resolution of 13.3 Hz. This is also the case for all following SPL spectra.
Nevertheless, the plots of Fig. 6 and Fig. 7 already demonstrate the influence of certain geometric parameters on the acoustic output. Particularly noteworthy in this context is the influence of the increased pitch value of the AP propeller. Despite having the smallest diameter, the AP propeller generates thrust comparable to the MP case, but the required torque to achieve this rotational velocity is significantly higher, which is reflected in the lower c_T/c_Q ratio. In terms of acoustic output,



(a) Directivity OASPL results (dB) in the XZ plane.



(b) SPL (dB) spectra - Observer at 90° in the XZ plane.

Figure 7 – Computational SPL spectrum and directivity plot for the scanned and rebuilt versions of the reference geometries operated at 4000 RPM and J = 0.

a higher pitch value leads to increased broadband noise, reflected in a higher OASPL contribution. This is consistent with findings from the literature, which focused on smaller propeller diameters [15]. Thus, at the same rotational velocity as the 24-inch TM propeller, which generates approximately 30 N more thrust, the 20-inch AP propeller achieves a similar total OASPL output. However, since the most efficient operating point differs for each of the investigated geometries, this relation of thrust to noise output can change significantly at different advance ratios and consequently rotational speeds. This once again emphasises the importance of using multiple reference geometries for this parameter study.

5.3 FEM structural analysis

For a comprehensive assessment of the experimental results, mechanical properties must also be taken into account. While only the tip deflection (δ_x) was experimentally verified, the maximum stresses (σ_{max}) and strains (ε_{max}) must also be analysed to ensure safe operation. In this context, it should be noted that the centrifugal forces and aerodynamic loads from the LBM simulations were applied to the initially undeformed geometries. No coupling of the simulation methods was implemented since the CFD and CAA processes are computationally expensive.

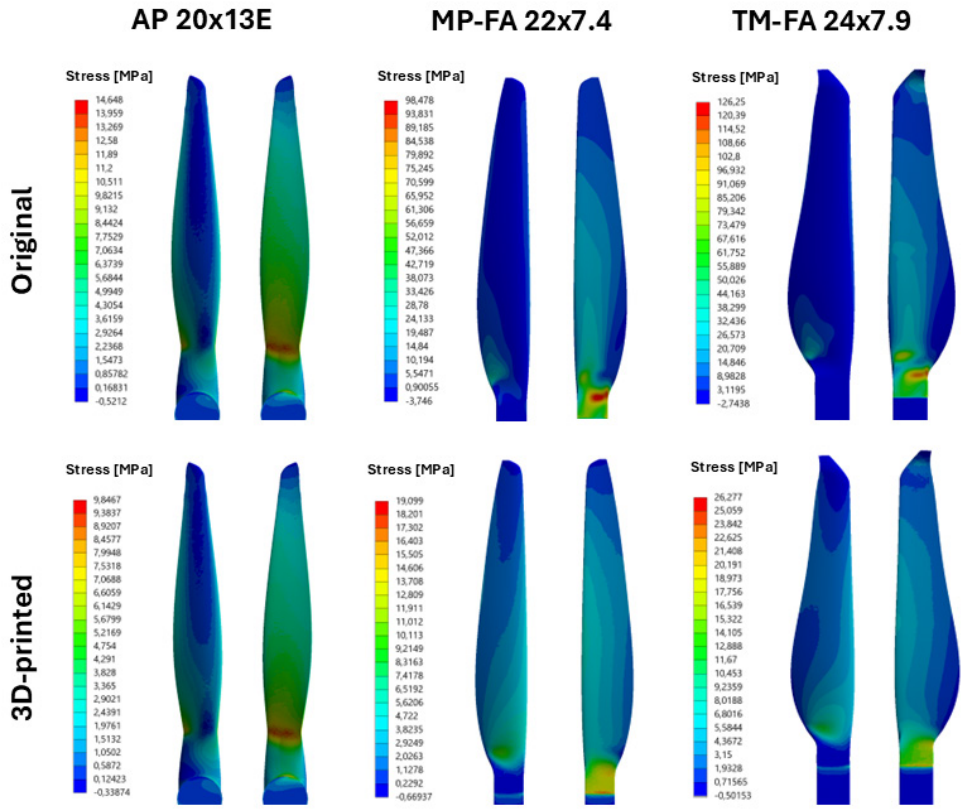
In Tab. 4, the computational tip deflections, maximum stress and maximum elastic strain data of the conventional propellers, compared to the experimentally obtained data at 4000 RPM and hovering conditions, are listed. While the tip deflections of the original propellers from the manufacturers remained low in both the computational study and the experiments, the bending of the 3D-printed PLA blades was clearly noticeable. Despite variations in geometric parameters and performance data, all three 3D-printed reference geometries exhibited similar deflections at the blade tip, which were approximately two times greater than for the injection-moulded material and four times greater than for the CFRP composite.

For the AP geometry, the maximum stress and consequently the maximum strain occurred on the pressure side of the blades, directly at the transition from the aerodynamic surfaces to the hub attachment structure, as seen in Fig. 8a. This is also the radial position at which the twist has its maximum and the respective gradient changes. When comparing the maximum elastic strain values for both cases, it can be seen that the PLA propeller results in more than twice the strain compared to the GF Nylon version. However, for both cases, the maximum stress remains relatively low. The MP-FA geometry shows the highest stress and strain areas near the support boundary conditions at the hub, mainly on the pressure side of the propeller, and at the trailing-edge, where the rectangular hub profile changes to the aerodynamic cross-section. A similar pattern was observed for the TM-FA geometry, as displayed in Fig. 8a. Despite the high strain values obtained, the limits listed in Tab. 2 were not exceeded for this operational point. The higher strain values of the PLA versions of these two reference geometries compared to the AP variant can be attributed to their thinner profiles and the correspondingly lower material volume.

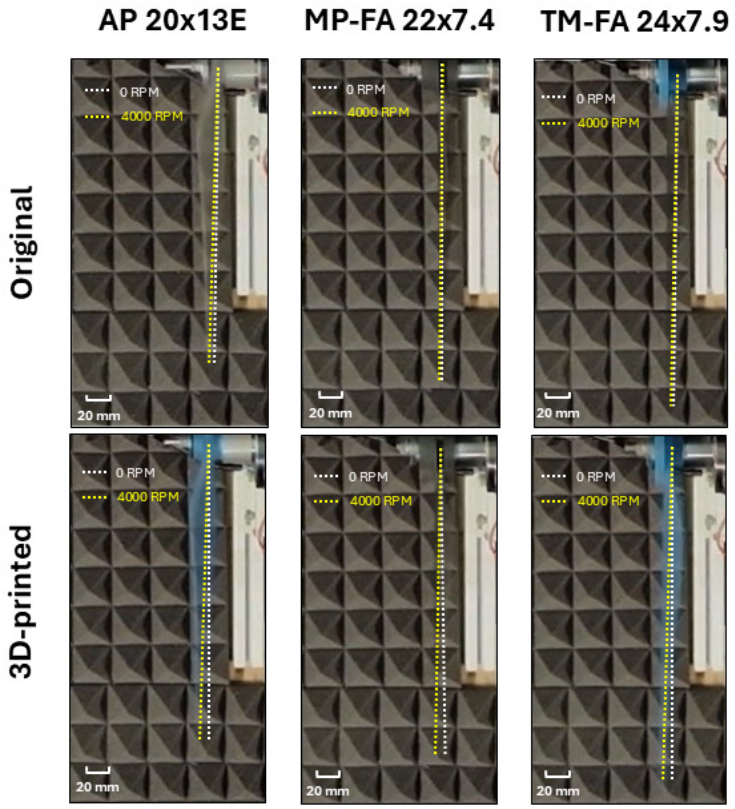
The experimentally obtained tip deflections of the original and 3D-printed propellers are shown in Fig. 8b. Since it is difficult to see the deflection of some of the blades due to little contrast with the absorbers in the background, dashed lines were added, which connect the hub to the current position of the tip. The white lines represent the initial state of the propeller without rotation, while the yellow lines capture the transition of the tip at 4000 RPM. For all 3D-printed PLA propeller blades, which

Table 4 – FEM and experimental results of conventional and 3D-printed propeller blades at 4000 RPM and J = 0.

Case	Computational			Experimental
	$\delta_x[mm]$	$\sigma_{max}[MPa]$	$\varepsilon_{max}[\%]$	$\delta_x[mm]$
AP original	5.14	14.09	0.17	~ 5
AP 3D-printed	10.58	9.46	0.41	~ 10
MP-FA original	2.59	98.48	0.17	~ 2
MP-FA 3D-printed	10.74	19.10	0.72	~ 10
TM-FA original	2.93	126.25	0.25	~ 2
TM-FA 3D-printed	10.81	26.28	0.92	~ 10



(a) FEM stress results on both sides of the blades.



(b) Experimental tip deflections of the original and 3D-printed propellers.

Figure 8 – Structural and mechanical properties based on computational and experimental results.

resulted in similar tip deflections of about 10 mm, the unmodified cases are shown in the figure. However, comparable data were obtained for the surface-treated models.
The tip deflections, as well as the relevant stress and strain data, were also calculated at 5000 RPM for the PLA cases to demonstrate that operating the 3D-printed blades at this rotational velocity is safe. Based on the maximum strain values, no failure is expected under these operating conditions for any of the geometries. However, the maximum stress value of the TM-FA 3D-printed propeller is approaching the yield strength, resulting in a safety factor of just over one.

6. Experimental campaign

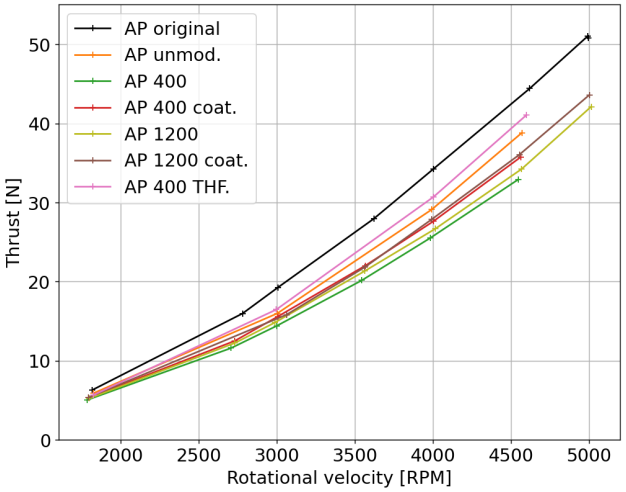
In this chapter, all results of the 3D-printed and post-processed propeller blades, compared to the original ones, are summarised. It must be noted at this point that it was not possible to operate some 3D-printed propellers at the predefined rotational speeds due to increased vibrations detected by the axial accelerometers. Despite static balancing efforts, careful propeller mounting, and the removal of sharp edges, safe operation of these propeller geometries at higher RPM could not be guaranteed. For this reason, for certain cases, results at higher rotational velocities are not available.

6.1 Aerodynamic performance

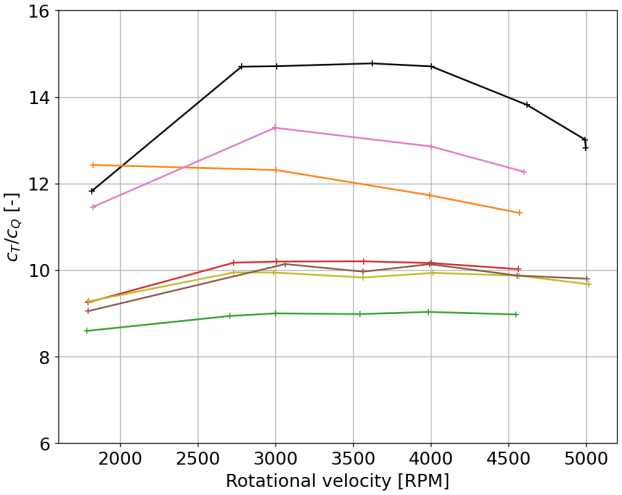
As expected, the thrust results of the PLA propellers indicate the aerodynamic penalty of 3D-printed blades in comparison to the original reference blades. This can clearly be seen in Fig. 9 (a),(c),(e) for the respective geometries, where the original propeller, indicated by the black line, outperforms the rest. However, it also becomes evident that post-processing can significantly improve the aerodynamic performance of the 3D-printed propellers, reducing the thrust gap relative to the original design. In the c_T/c_Q plots, which are given in Fig. 9 (b),(d),(f), some post-processed geometries even outperformed the conventional baseline propellers.
Surprisingly, the unmodified AP 3D-printed propeller resulted in higher thrust and c_T/c_Q data than most of the surface-treated propellers, independent of the operational state. Only the chemically treated version achieved slightly better performance, as shown in Fig. 9a. Since these two versions are the only clockwise rotating propellers, those results could also be linked to the asymmetric recirculation patterns in the experimental setup. However, when excluding them, it becomes clear that the two coated propellers performed better than the blades which were only sanded.
This also becomes evident when looking at the MP-FA geometries in Fig. 9c, where the two coated blades outperform the others and almost match the thrust of the original propeller. Based on the c_T/c_Q ratio, it can also be seen that these two variants achieve higher values than the conventional one at all rotational speeds, followed by the THF-treated blades (see Fig. 9d). For the TM-FA propellers, the unmodified 3D-printed variant clearly shows the worst performance output, with thrust losses of up to 11 N (see Fig. 9e). The ratio of thrust-to-torque coefficients is also significantly lower for this geometry. Once again, the two coated versions rank highest, as shown in Fig. 9f, followed by the chemically treated variant, with all of them outperforming the conventional propeller. In terms of thrust, however, the opposite can be seen and the gap is more pronounced than for the MP-FA geometry.
Although the thrust gap to the conventional propellers can be significantly reduced in some cases by means of surface treatment, it is not realistic to achieve equivalent performance for several reasons. The primary reason for this is the different materials used and the resulting variations in stiffness. In addition to the already demonstrated significantly greater deflection of the 3D-printed cases under load, increased torsional twisting of the profiles is also to be expected at higher rotational speeds, which causes the angle of attack to change, particularly in the outer radial sections. The shift in the aerodynamic operating point is also represented by the c_T/c_Q ratio improvements of the PLA propellers.

6.2 Acoustic results

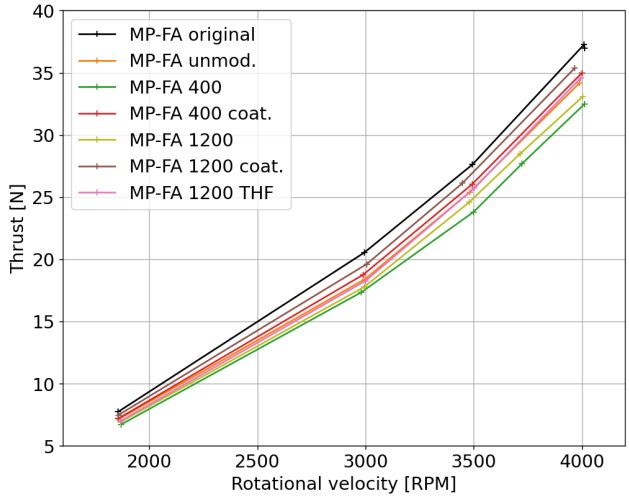
Finally, the acoustic results are presented in this chapter. For each of the reference geometries, the directivity pattern as well as the SPL spectrum for an observer at 90° in the rotational plane are displayed. In order to visualise the data in a compact way, only the results of those cases, which show lower noise output than the conventional geometry in the directivity graph, are displayed in the SPL



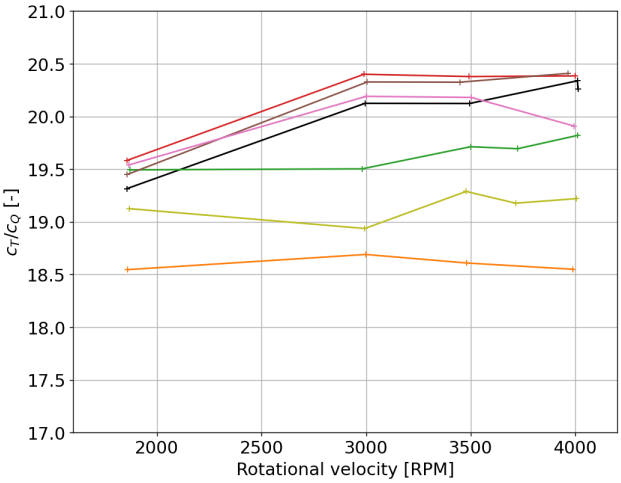
(a) Thrust results of AP geometries.



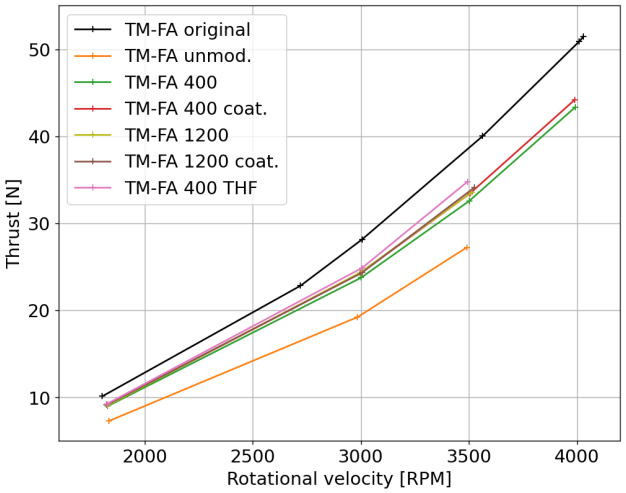
(b) c_T/c_Q results of AP geometries.



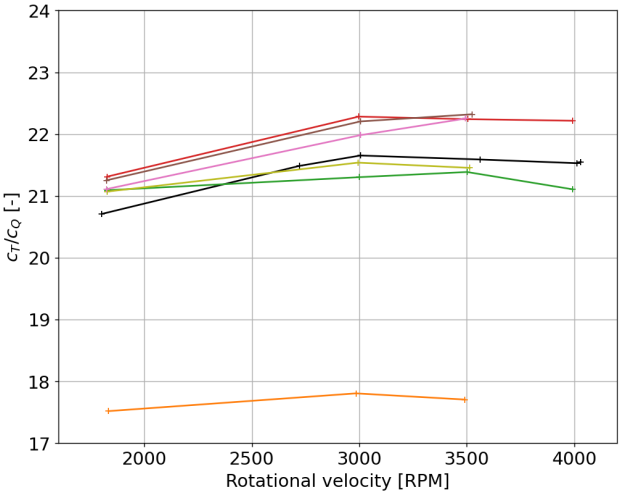
(c) Thrust results of MP-FA geometries.



(d) c_T/c_Q results of MP-FA geometries.



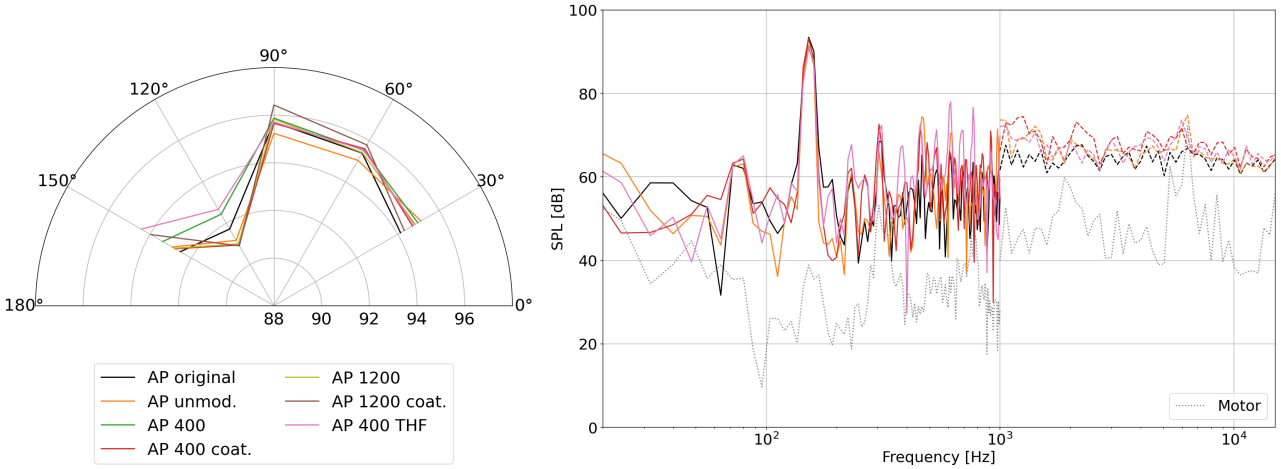
(e) Thrust results of TM-FA geometries.



(f) c_T/c_Q results of TM-FA geometries.

Figure 9 – Experimental performance data: Thrust and c_T/c_Q plotted over RPM.

spectrum. Furthermore, based on the aerodynamic performance outputs, different rotational velocities were selected for each propeller geometry to display results at multiple operational points.
The strong correlation between aerodynamic and aeroacoustic effects, as well as the corresponding dependency, becomes evident when analysing the directivity plot for the AP propellers at 4500 RPM, as shown in Fig. 10a. Similar to the thrust and c_T/c_Q graphs, it can be seen that once again the unmodified geometry performs best. The small OASPL reduction in the rotational plane is also evident in the corresponding SPL spectrum, displayed in Fig. 10b. Especially at the first BPF, a lower noise output than the conventional reference blade is achieved. However, at frequencies above 1 kHz, the baseline propeller shows the lowest broadband noise emissions. At this point, it should also be noted that some components of the frequency spectrum can also be attributed to the motor noise. For the respective rotational speed, the noise was determined in advance. In this case, for example, the noise of the motor is accountable for the peak at approximately 7 kHz.

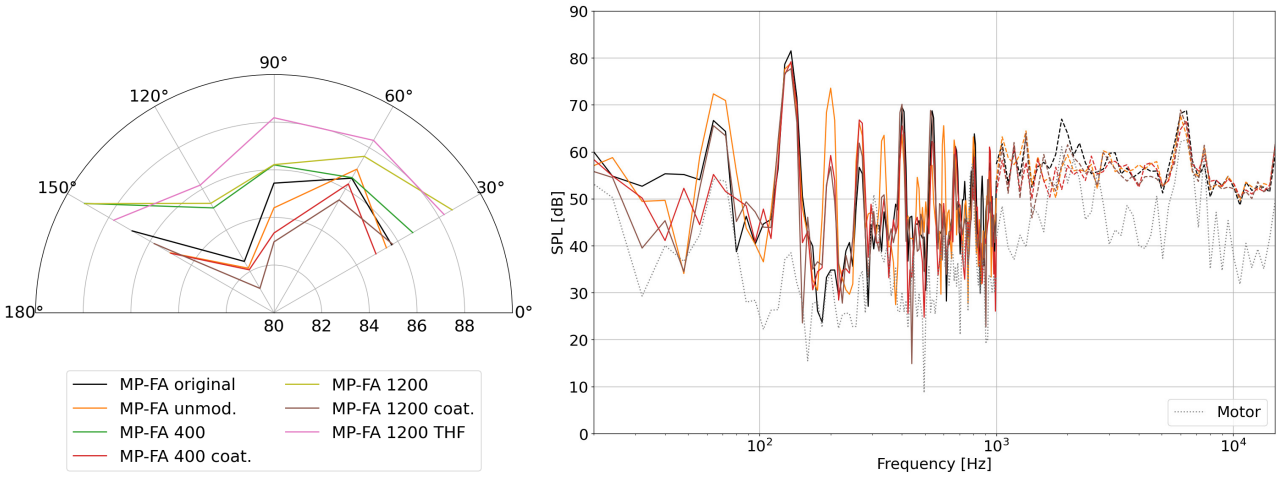


(a) Directivity in OASPL (dB) on plane XZ.

(b) SPL (dB) spectra - Observer at 90° on plane XZ.

Figure 10 – SPL spectra and directivity plot for the AP propellers operated at 4500 RPM and J = 0.

The relevance of considering multiple propellers in this parameter study with different geometric characteristics, such as diameter, pitch, chord length as well as twist distribution, is highlighted by the significant variations in the directivity patterns shown in Fig. 11a. In contrast to the AP propeller, the chemically treated version performs below expectations in this instance. However, it must be noted that for this geometry, the 1200-grit sanded version was processed with THF instead of the 400-grit variant, which was used for the other two propellers. Furthermore, both sanded-only variants achieved higher OASPL values for nearly all microphone positions than the conventional propeller. Since these blades again performed worse than the unmodified ones taken directly from the printer, they are not included in the SPL spectrum for an observer in the plane of rotation. Both coated versions outperformed the rest, with the variant treated with 1200-grit sandpaper achieving the lowest overall noise emissions, with a reduction of up to 2.5 dB compared to the conventional propeller.
Similar to the AP geometry, the noise reductions can be attributed to a lower tonal output at the first BPF and an attenuation of broadband noise between 1 kHz and 2 kHz, as shown in Fig. 11b. Particularly interesting and clearly visible in the frequency spectrum are the tonal peaks that occur at 200 Hz (corresponding to 1.5 BPF) and at 333 Hz (equivalent to 2.5 BPF) for the 3D-printed propellers. The original CFRP blade shows either no amplitude or only a minimal one at these frequencies. These are indications of periodic load fluctuations, which are usually caused by asymmetries or manufacturing variations. Sub-frequencies can also be amplified due to vibrations and corresponding resonances. These factors also explain the reduction in tonal noise at the integer BPFs, as the tonal noise subsequently appears as sub-harmonics.
The directivity pattern for the largest propeller in terms of diameter and solidity, namely the TM-FA geometry, is displayed in Fig. 12a. Since the accelerometer fluctuations and consequently the vi-



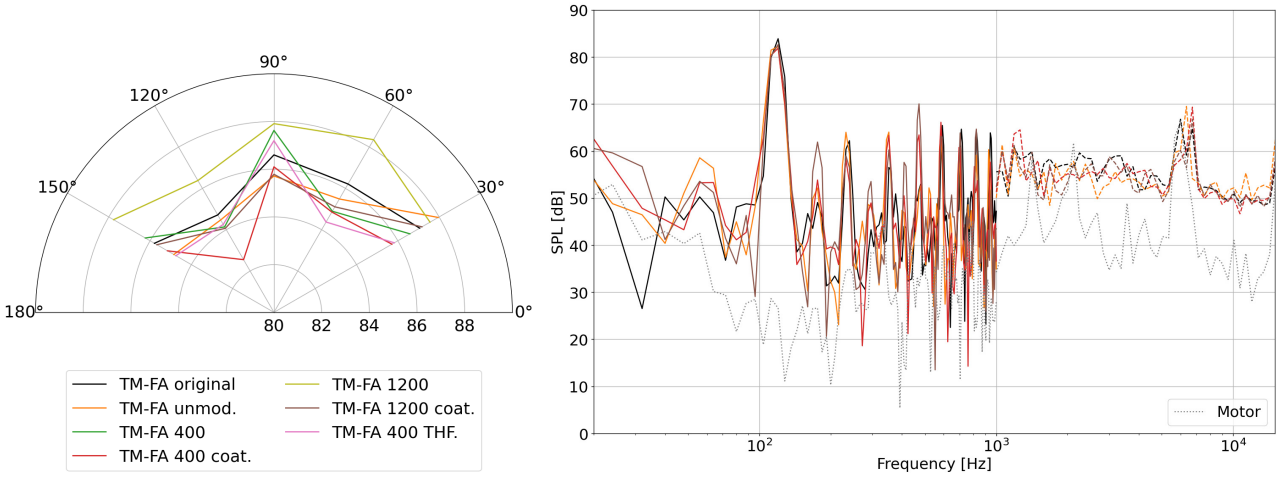
(a) Directivity in OASPL (dB) on plane XZ.

(b) SPL (dB) spectra - Observer at 90° on plane XZ.

Figure 11 – SPL spectra and directivity plot for the MP-FA propellers operated at 4000 RPM and J = 0.

brations during the operation of some of the 3D-printed versions exceeded the safety limits for an operation at 4000 RPM, it was decided to compare the noise output data at 3500 RPM. The OASPL results of most of the post-processed geometries are lower than the conventional CFRP propeller at several of the five microphone positions. Nevertheless, it is evident that the best overall output was achieved by the 400-grit coated version, closely followed by the 1200-grit coated variant and the unmodified 3D-printed propeller. These cases are also shown in the SPL spectrum in Fig. 12b for a more detailed assessment. The remaining geometries also resulted in partial noise reduction compared to the original propeller, except for the 1200-grit-sanded version, which confirms that sanding alone is not sufficient.

The frequency spectrum, displayed in Fig. 12b, once again reflects the findings from the two previously examined geometries, although the half-BPFs are less pronounced for this geometry. However, this could also be related to the different operating conditions. Since the OASPL reductions in the rotational plane between the variants shown and the original propeller are less than 1 dB, further differences in the spectrum are difficult to identify. As already stated in the aerodynamic performance



(a) Directivity in OASPL (dB) on plane XZ.

(b) SPL (dB) spectra - Observer at 90° on plane XZ.

Figure 12 – SPL spectra and directivity plot for the TM-FA propellers operated at 3500 RPM and J = 0.

chapter, one of the reasons for the noise reductions achieved here is the variation in the effective angle of attack caused by torsional twisting. Moreover, in this chapter, a direct comparison at the same rotational speed was intentionally presented. When comparing the cases based on a reference thrust value, the PLA propellers are expected to generate significantly higher noise levels than the conventional versions.
To conclude, in Fig. 13, the OASPL changes referred to the conventional propellers recorded at the microphone positioned directly above the propeller at 90° are shown for all experimentally tested propellers at various rotational speeds. The two particularly promising cases of the AP Geometry, which showed aerodynamic performance improvements, namely AP unmod. and AP 400 THF, clearly result in significantly higher OASPL output than the baseline propeller at an operating point of 3000 RPM. In general, the only noteworthy reductions in OASPL for this geometry compared to the conventional propeller were achieved at 4500 RPM. In all other operating conditions, every post-processed version generated a higher OASPL output than the injection-moulded propeller.
In the case of the MP-FA geometry, for which the output at 4000 RPM has already been plotted, it can be seen that the coated version, which was sanded to 400 grit beforehand, could also achieve a reduction in OASPL at the other two operating points. While the remaining surface-treated cases were partially able to decrease the OASPL output, some of them also resulted in an increase. A similar observation can be made regarding the TM-FA geometry, although in this case the unmodified and 1200-coated cases also provided positive outcomes.

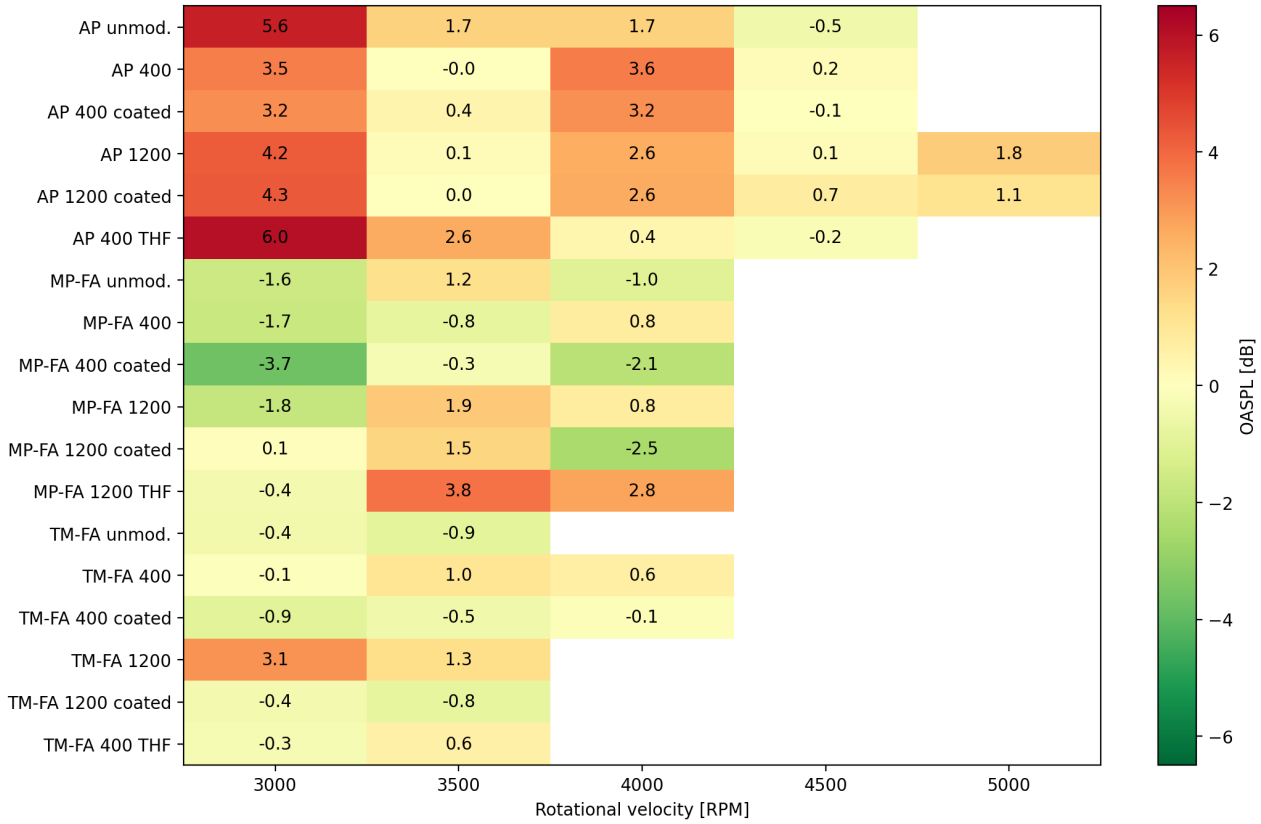


Figure 13 – OASPL data in the rotational plane at multiple RPM referred to the respective conventional propeller results.

7. Conclusion

In this study, three commercially available reference propellers with different geometrical parameter combinations were computationally and experimentally evaluated to demonstrate that 3D-printed propeller blades can represent a viable and highly flexible solution for rapid prototyping in AAM research activities. The computationally obtained aerodynamic and acoustic data served as a baseline for the experimental campaign. The structural assessment using FEM simulations contributed to ensuring

safe operation by analysing the maximum stress and strain data, and enabled comparison of the tip deflections with the experimentally determined data. The 3D-printed PLA blades were modified using multiple surface treatment techniques, including sanding, spray coating and chemical treatment with THF. For each conventional propeller geometry, six post-processed versions were tested in the sound measurement room. Although the PLA-printed propellers exhibited certain aerodynamic performance penalties compared to the original blades, improvements in the thrust-to-torque ratio (c_T/c_Q) and, in some cases, reduced acoustic emissions were observed. This study further showed that surface post-processing plays a decisive role in the final performance. Among the evaluated methods, sanding up to 400 grit, followed by spray coating, provided the best overall aerodynamic and acoustic results while achieving surface roughness close to that of commercially manufactured propellers. Nevertheless, several practical limitations remain. Issues with hub connections, especially for foldable propellers, have introduced dimensional inaccuracies, suggesting that inserts or alternative connection concepts are necessary. Furthermore, vibrations occurred during testing despite static balancing, limiting achievable rotational speeds and reducing suitability for sustained high-load operation. In addition, the required post-processing effort remains considerable and partially offsets the manufacturing speed advantage.

Overall, 3D-printed propeller blades fulfil their primary purpose as rapid prototyping tools by enabling fast, cost-effective experimental validation without the high investment associated with injection moulding or CFRP manufacturing processes. While the investigated blades are suitable for short-term testing and design iteration, their current limitations in structural integrity, vibration behaviour, and durability make 3D-printed propellers within this diameter range unsuitable for long-term operational use. Future work should therefore focus on compensating for deformation effects related to torsional twisting, with the goal of achieving equivalent thrust performance to reference propellers while maintaining the manufacturing advantages of additive production.

Contact Author Email Address

Author: Dominik Skrna, PhD candidate at TU Wien
E-mail: dominik.skrna@tuwien.ac.at

Copyright Statement

The authors confirm that they, and/or their company or organisation, hold copyright on all of the original material included in this paper. The authors also confirm that they have obtained permission, from the copyright holder of any third party material included in this paper, to publish it as part of their paper. The authors confirm that they give permission, or have obtained permission from the copyright holder of this paper, for the publication and distribution of this paper as part of the ICAS proceedings or as individual off-prints from the proceedings.

Acknowledgements

The research presented in this publication has been conducted by the Aircraft Systems Research Group of the Technische Universität Wien. The research group receives funding from the Austrian Aviation Programme TAKE OFF via the BMIMI Endowed Professorship for Innovative Aviation Technologies. This research is also associated to the project NeoBlade, funded by FFG via TAKE OFF.

The fundamental work, on which this paper is based on, was carried out by three mechanical engineering students as part of individual seminar papers within the framework of the Aircraft Design Seminar in the winter semester 2025/26. The authors would like to sincerely thank the Research Group for Production Metrology and Adaptronic Systems and the Research Unit of Tribology for their valuable support in providing the 3D scan data and surface roughness measurements essential to this work. The computational simulations have been conducted with the Austrian Scientific Computing (ASC) cluster infrastructure.

References

[1] Popister F, Goia H S, and Ciudin P. Influence of polymers surface roughness on noise emissions in 3D-printed UAV propellers. *Polymers*, 17(8):1015, 2025.

[2] Hood M J. The effect of surface irregularities on wing drag: Roughness - 3.

[3] Chiusoli R Z. Experimental study of modifications of drone propeller blades for noise reduction and performance. Master's thesis, Tecnico Lisboa, 2022.

[4] Toleos L R, Luna N J A B D, Manuel M C E, Chua J M R, Sangalang E M A, and So P C. Feasibility study for fused deposition modeling (FDM) 3D-printed propellers for unmanned aerial vehicles. *Int. J. Mech. Eng. Robot. Res.*, pages 548–558, 2020.

[5] García-Tíscar J, Quintero P, Varela P, Ramírez F N, and Cremades A. On the effect of popular additive manufacturing technologies on the performance and noise emission of UAV propellers. *Aerospace Science and Technology*, 169:111466, 2026.

[6] Dizon J R C, Gache C C L, Cascolan H M S, Cancino L T, and Advincula R C. Post-processing of 3D-printed polymers. *Technologies*, 9(3):61, 2021.

[7] Takagishi K and Umezu S. Development of the improving process for the 3D printed structure. *Scientific Reports*, 7(1):39852, 2017.

[8] Mathew A, Kishore S R, Tomy A T, Sugavaneswaran M, Scholz S G, Elkaseer A, Wilson V H, and John Rajan A. Vapour polishing of fused deposition modelling (FDM) parts: a critical review of different techniques, and subsequent surface finish and mechanical properties of the post-processed 3D-printed parts. *Progress in Additive Manufacturing*, 8(6):1161–1178, 2023.

[9] Advanced Precision Composites. APC model aircraft propellers - manufacturing.

[10] ANSYS, Inc. Granta materials data, 2026.

[11] Prusa Polymers a.s. Technical datasheet - Prusament PLA by Prusa Polymers.

[12] DIN EN ISO 527-2:2012-06, Kunststoffe - Bestimmung der Zugeigenschaften - Teil 2: Prüfbedingungen für Form- und Extrusionsmassen (ISO 527-2:2012); Deutsche Fassung EN ISO 527-2:2012.

[13] *PowerFLOW 2022 user's guide*. Dassault Systèmes Simulia Corp, 2022.

[14] Grande E, Ragni D, Avallone F, and Casalino D. Laminar separation bubble noise on a propeller operating at low Reynolds number. *AIAA Journal*, 60:5324–5335, 2022.

[15] Pang E, Cambray A, Rezgui D, Azarpeyvand M, and Showkat A S A. Investigation towards a better understanding of noise generation from UAV propellers. In *2018 AIAA/CEAS Aeroacoustics Conference*. American Institute of Aeronautics and Astronautics.